Supporting Information

Growth dynamics and photoresponse of Wadsley phase V_6O_{13} crystal

Wen Zeng[1#], Xiaoguo Fu[4#], Li Yu[2], Tingting Shi[1], Pengyi Liu[1], Jianbin Xu[5,6], Jian Chen[6,7], Qiulan Chen[3]*, Xiaomu Wang[2]*, Weiguang Xie[1, 6]*

1. Siyuan Laboratory, Guangdong Provincial Engineering Technology Research Center of Vacuum Coating Technologies and New Energy Materials, Department of Physics, Jinan University, Guangzhou, Guangdong 510632, China.
2. School of Electronic Science and Technology, Nanjing University, Nanjing, Jiangsu 210093, China
3. Department of Medical Devices, Guangdong Food and Drug Vocational College, Guangzhou, Guangdong 510520, China
4. Science and Technology on Surface Physics, and Chemistry Laboratory, Mianyang, Sichuan, 621908, China,
5. Department of Electronic Engineering and Materials Science and Technology Research Center, the Chinese University of Hong Kong, Hong Kong SAR, China
6. State Key Laboratory of Optoelectronic Materials and Technologies, Sun Yat-sen University, Guangzhou, Guangdong 510275, China
7. Instrumental Analysis & Research Center, Sun Yat-sen University, Guangzhou, Guangdong 510275, China

* Author to whom correspondence should be contact: QL Chen: chenql@gdyzy.edu.cn ;XM Wang: xiaomu.wang@nju.edu.cn ; WG Xie: wgxie@email.jnu.edu.cn
# These authors contribute equally to this work

The home-built heating stage for monitoring growth in situ

We designed a compact high-temperature heating stage according to the design of E. Strelcov.[1] The heating stage allows heating temperature exceeding 1000 °C under a microscope with telephoto lens (up to 1000× and working distance around 1 cm) for in-situ investigation, as shown in **Figure S1**. The home-built heating stage is based on direct current heating of a tungsten sheet connected between two copper electrodes. The sample is placed on the tungsten sheet for heating. A thermocouple is attached to the sample that allowed local temperature measurement. A PID temperature controller is used to tune the sample temperature during heating. The heating unit is sealed in the small vacuum chamber. The chamber is water-cooling through the cooling inlet during the heating.

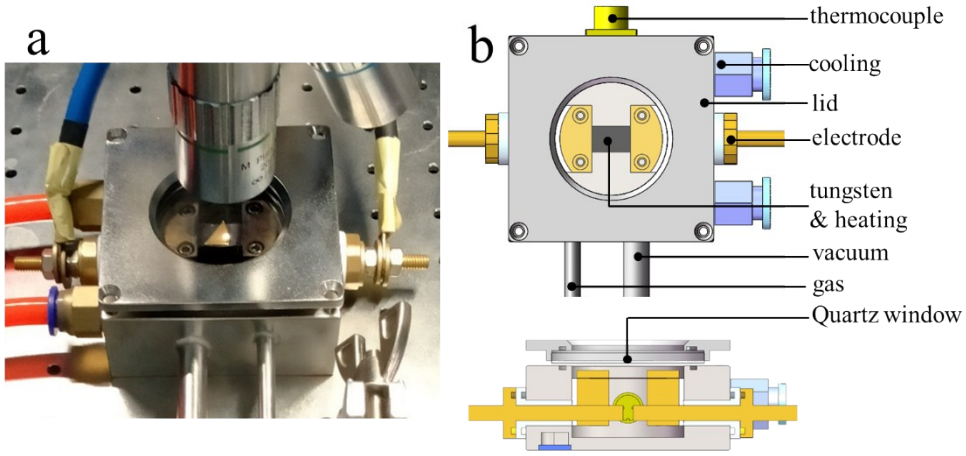

Figure S1. Home-built heating stage for in-situ investigation: (a) Picture of the heating stage under an optical microscope for real-time observation. (b) Top view and section view of the heating stage.

Morphology and structural characterization of V_6O_{13}

The phases of the precursor and the product were analyzed by Raman spectroscopy, and the results are shown in **Figure S2**. The precursor film prepared by drop casting method was a uniform orange film composed of V_2O_5 powders (**Figure S2**a). Compared with spin coating, doctor coating and spraying method, the above drop casting method was more convenient and simpler to operate that allows the preparation

of large-scale precursor film. After annealing at 700 °C for 180 minutes, a large number of millimeter-sized single crystals were grown on the substrate as shown in **Figure S2**b. The Raman spectrum in **Figure S2**c indicated that the products were pure V_6O_{13}.[2] Here, we have found that by controlling the concentration of the precursor solution, the crystal size of the grown V_6O_{13} can be well modulated, as shown in **Figure S2**d.

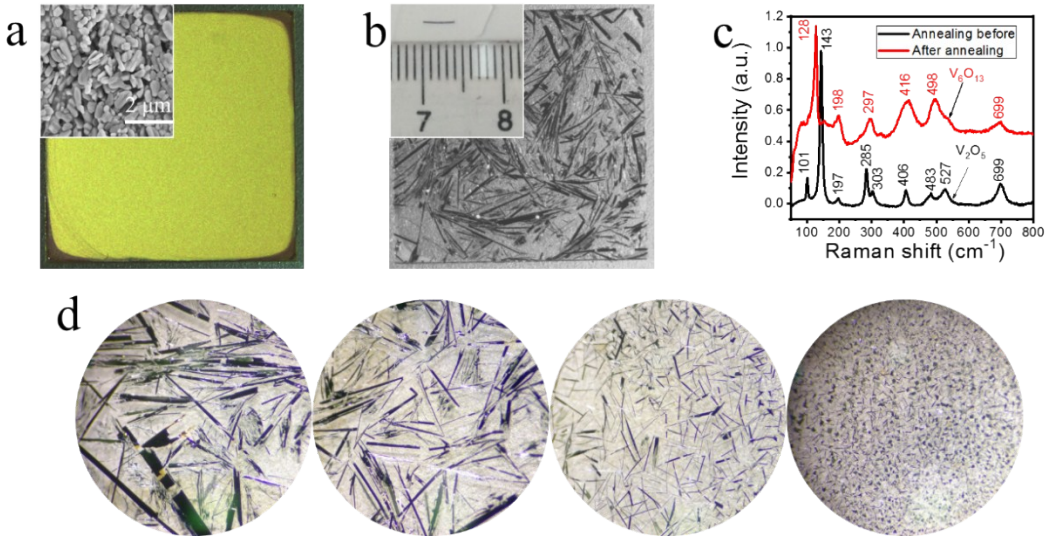

Figure S2. Morphology and Raman spectra before and after annealing of V_2O_5 precursor film. (a) The optical picture of as-prepared V_2O_5 precursor film. The sample substrate was a 10 × 10 mm sapphire. The inset shows the corresponding SEM morphology. (b) The optical picture of annealed product using sample in (a). (c) Raman spectra of samples before and after annealing. (d) Optical microscopic images of V_6O_{13} crystals grown by precursor solutions at concentrations of 0.18 mol/L, 0.09 mol/L, 0.06 mol/L, and 0.045 mol/L, respectively. The magnification is 5×.

XPS analysis of V_6O_{13}

The XPS spectrum of the grown single crystal (**Figure S3**a-c) shows that the binding energies of V $2p_{1/2}$ and V $2p_{3/2}$ are located at 523.9 eV and 516.6 eV, respectively, corresponding to the binding energy of the V_6O_{13} V2p orbital; and the peak fitting analysis of the V2p peak showed that the ratio of the area of V^{5+} and V^{4+} was 0.49, close to the valence ratio of 0.5 in V_6O_{13}. As shows in **Figure S3**c, the valence band of

the V_6O_{13} mainly comes from the contribution of V3d and O2p state.[3, 4] The tail of the valence band crosses the Fermi level. Our XPS results are consistent with the XPS result of V6O13 crystal in literatures. [4]

Figure S3d shows that after several days of storage in air, significant increase of the contamination band of O1s (indicated by red arrows) was observed. However, the ratio of V^{5+}/V^{4+} slightly increases to 0.51. (**Figure S3**e). A slightly shifting of VB band away from the Fermi level was observed (**Figure S3**f). This indicates that first, oxidation may appear, but it is still weak. Second, the surface absorption leads to a slight depletion on the surface. Caution should be taken to minimize the surface effect during storage and measurement.

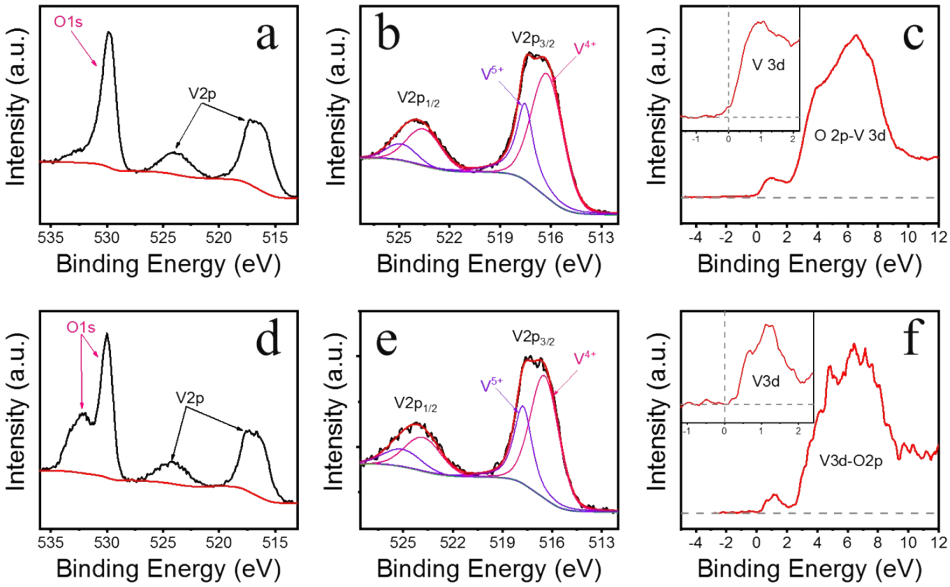

Figure S3. XPS spectra of V_6O_{13}. (a)-(c) O1s, V2p with fitting and valanced band spectrum of as-prepared V_6O_{13}, respectively. (d-f) O1s, V2p with fitting, and valanced band spectrum of V_6O_{13} after a long-term storage, respectively.

Temperature-resistance characteristics

In order to test the temperature resistance characteristics of the grown V_6O_{13} and determine its metal-insulation phase transition (MIT) temperature, we tested the resistance of V_6O_{13} crystal sheet with temperature at low temperature and room temperature, respectively, and calculated the TCR as shown in **Figure S4**.

Figure S4a, shows that at low temperature, the resistance of V_6O_{13} decreases sharply

with temperature by more than 3 order of magnitude. It can be clearly seen that near 150 K, there is an abrupt resistance change. This is consistent with the MIT temperature of V_6O_{13} in previous reports.[5] However, a wide temperature range for a large resistance change of 3 order of magnitude may imply that there are some effects, for example defect due to the slipping between adjacent layer, have affect the MIT behavior. It requires further investigation. The temperature-dependent resistance behavior has been utilized in room temperature infrared bolometric photodetectors. Such detectors utilize the change of resistance induced by infrared heating radiation. The main parameter to achieve high sensitivity of infrared bolometer is the temperature coefficient of resistance TCR, which is defined as:[6]

$$TCR = \frac{1}{R}\frac{dR}{dT} \qquad (1)$$

where R is the resistance and T is the temperature.

The TCR value of V_6O_{13} near room temperature was shown in **Figure S4**b. The TCR value at 300 K is only 0.6% K^{-1}, which is much lower than commercialized VO_x.

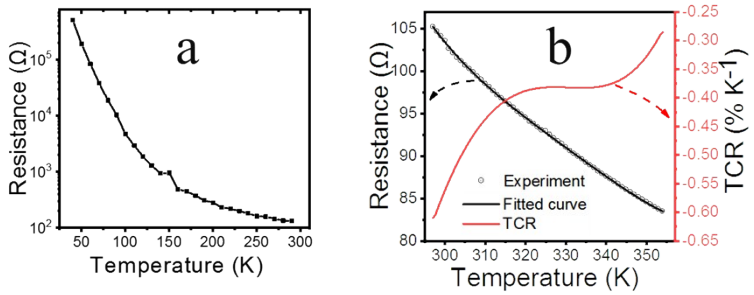

Figure S4. Temperature-resistance characteristic of V_6O_{13} crystal. (a) Low temperature, (b) above room temperature.

Characterization of mesophase structure

To identify the phase transition during the growth, we terminated the growth when the system was under typical transition processes in the in-situ experiments in **Figure 3**. The sample was quickly cooled down to room temperature and was subjected to SEM and Raman characterization. It's assumed that the chemical composition remained unchanged after cooling. The results are shown in **Figure S5**. The panels a-d in **Figure S5** correspond to the topographical maps of the critical phase transition in the panels 1,

2, 4, 6 in **Figure 3**, respectively. During the heating process, the orange precursor film gradually darkened, and the blackened precursor film remains black after cooling (**Figure S5**a-b & panel 2 of **Figure 3**), Raman spectroscopy proves that the phase is still V_2O_5. The SEM illustration in **Figure S5**a&b shows that the particle size is substantially identical to the unannealed precursor, indicating that the chemical reaction is gradual .[7] **Figure S5**c shows the corresponding topographical view after cooling in the state of panel 4 of **Figure 3**, the corresponding SEM image in **Figure S5**c shows the formation of nanorods after cooling of the solid-liquid blend phase; Raman spectroscopy identified mainly V_2O_5 with a small signal of V_6O_{13}, this indicates that when the precursor begins to melt, part of V_2O_5 began to decompose into V_6O_{13}. **Figure S5**d shows the P2' corresponds to the melt, and P1' corresponds to the newly appearing single crystal in the melt in panel 6 of **Figure 3**, the morphology of the two does not seem to match, this is because the melt will crystallize under too cold,[8] Raman spectroscopy identified the melt as V_2O_5 and the newly emerging single crystal was V_6O_{13}.

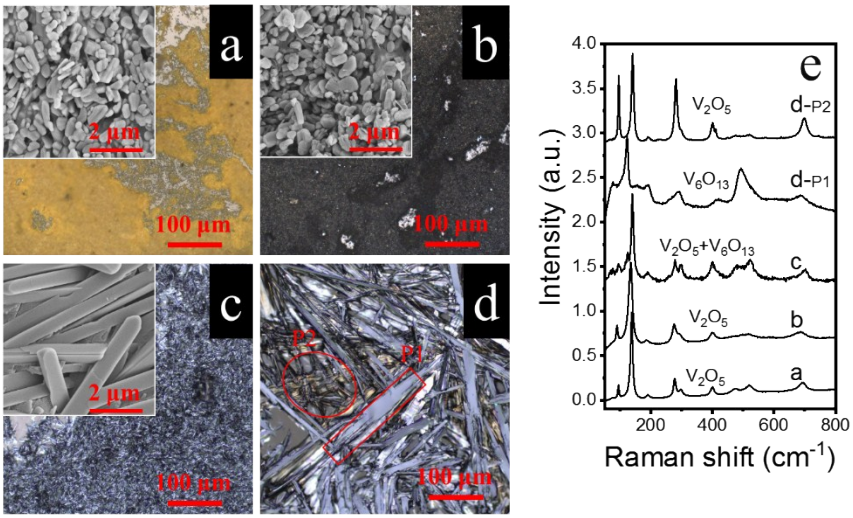

Figure S5. Morphology and Raman spectroscopy of the key phase transition stages in Figure 3 during in-situ growth. (a-d) are the optical microscope image corresponding to the process the panels 1, 2, 4, 6 in Figure 3, respectively. Each inset shows the corresponding SEM image. (e) Corresponding Raman spectra in (a-b).

A quasi-situ growth experiment was carried out in a tube furnace to further illustrate the evolution process from V_2O_5 precursor to V_6O_{13} crystal sheet. The V_2O_5 precursor films were placed in a tube furnace. The samples were heated to 600, 675, and 700 ℃ at a heating rate of 15 ℃/min in a vacuum of 5 Pa , respectively, at each temperature, the sample was annealed for 5 minutes, the sample was then naturally cooled down and taken out for XRD characterization. **Figure S6** shows that when the temperature is not higher than 600 ℃, the film is composed of pure V_2O_5 phase; when the temperature reached 675 ℃, small (*00l*) peaks of V_6O_{13} was observed, it implied that the reduction of V_2O_5 started; The XRD intensity of V_6O_{13} gradually increases with the increase of temperature and time, which is consistent with the results of the above in-situ investigation. With prolong annealing at 700 ℃ for 180 min, V_2O_5 was completely removed, and a pure V_6O_{13} phase remained. From a chemical point of view, the growth can be described as the thermal reduction of V_2O_5 along the following route:

$$3V_2O_5(l) \rightarrow V_6O_{13}(s) + O_2(g)$$

where the *s*, *l* and *g* indicators represent the solid phase, the liquid phase and the gas phase, respectively.[9]

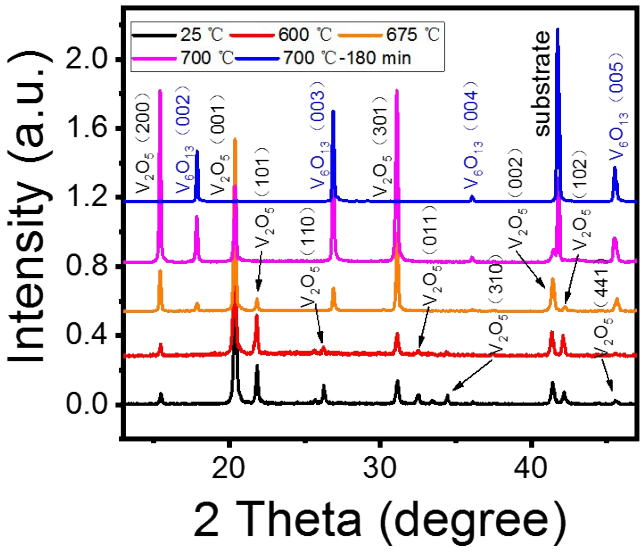

Figure S6. The quasi-situ XRD spectra evolution during the growth of V_6O_{13} crystal.

Photoresponse test and calculation of V_6O_{13}

Figure S7a shows the I–V curves of the photodetector at room temperature in the dark (black curve) and under laser illumination with the intensity of 23.66 μW (red curve), respectively. The I-V curve shows non-linear behavior in bias range of -0.5V to 0.5V, which implies the formation of a Schottky contact between the Au electrode and the V_6O_{13} crystal. From the KPFM test in **Figure S7**b, we can clearly see that a 38.9mW surface contact potential difference exists.

Responsivity (R), External quantum efficiency (EQE), and Detectability (D*) important parameters for evaluating the performance of photodetectors. Responsivity is the efficiency with which the device converts light into photocurrent and can be calculated as[10]:

$$R_\lambda = \frac{\Delta I}{P} \qquad (2)$$

where ΔI is the photocurrent, and P is the effective optical power of the laser injection. When the R value is calculated, the corresponding EQE value can be calculated as[11]:

$$EQE = \frac{R_\lambda hc}{\lambda e} \qquad (3)$$

where h is Planck's constant, c represents the velocity of light, λ denotes the light wavelength, and e is the electron charge. The device has a high responsivity of 100 A/W and high EQE of 5.4×10^4 % at 0.02 μW with a small bias voltage of 0.1 V under 405 nm illumination are shown in **Figures 5**d.

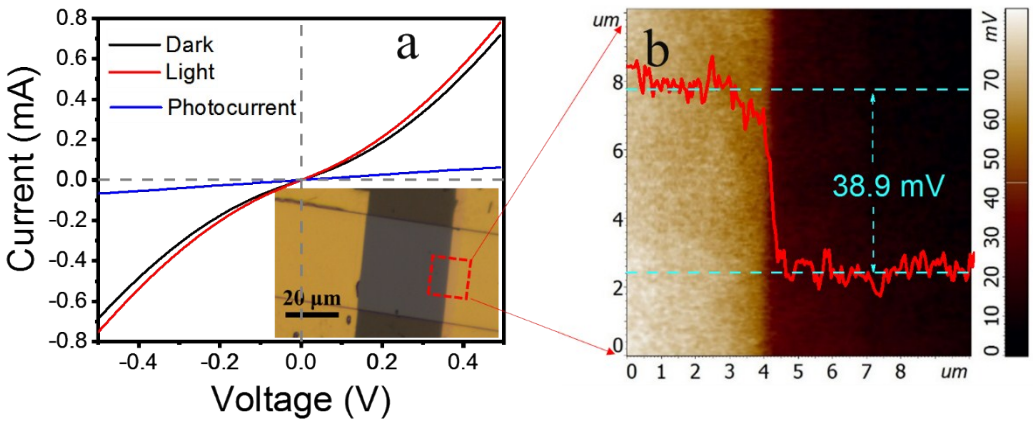

Figure S7. (a) The I-V curves of the device in darkness and illumination (Laser with a wavelength of 405 nm). Insert shows the microscope picture of the device. (b) KPFM surface potential image at the Au/V_6O_{13} contact illustrated as a dotted box in (a).

At the contact, the photocurrent can generate due to the photoelectric effect from the contact potential difference (V_{CPD}) of 38.9 meV from the KPFM result. It can also generate due to the photothermoelectric effect, and the voltage generated is given by

$$\Delta V_{PTE} = (S_{semiconductor} - S_{metal}) \cdot \Delta T$$

As the Seebeck coefficient of V_6O_{13} is around -20 μV/K[12] and gold is < 1 μV/K. It can be seemed that even with the local temperature of 720 °C (melting point of V_6O_{13}), ΔVPTE is still much smaller than the V_{CPD}. As no structural and electrical change were observed after photoresponse measurement, the local temperature should not be so high and photothermalelectric effect should not dominate the photoresponse behavior at the contact.

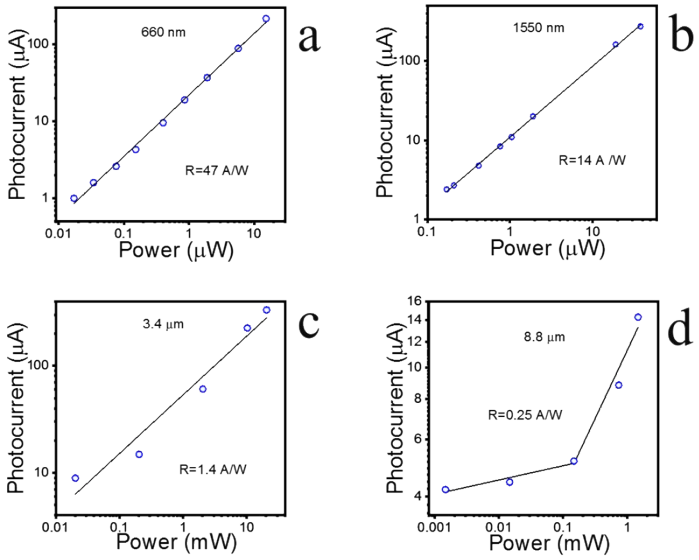

Figure S8. Power dependent photoresponse characteristics under illumination of (a) 660 nm, (b) 1550 nm, (c) 3.4 μm and (d) 8.8 μm.

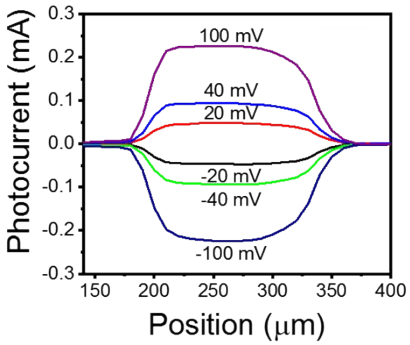

Figure S10. The photocurrent line profiles without the contact effect in b, that is, all lines are deducted from the spatial photocurrent line profile under zero bias. The calculated G_{ph} was given in Figure 6c.

Support Material Video 1： In-situ monitoring of growth

Support Material Video 2：Melt-driven pyrolysis growth mechanism

Support Material Video 3：Modification of the wetting layer

References

1. E. Strelcov, A. V. Davydov, U. Lanke, C. Watts and A. Kolmakov, *ACS nano*, 2011, **5**, 3373-3384.
2. X. Wang, H. Li, Y. Fei, X. Wang, Y. Xiong, Y. Nie and K. Feng, *Applied Surface Science*, 2001, **177**, 8-14.
3. T. Schmitt, L. C. Duda, M. Matsubara, M. Mattesini, M. Klemm, A. Augustsson, J. H. Guo, T. Uozumi, S. Horn, R. Ahuja, A. Kotani and J. Nordgren, *Physical Review B*, 2004, **69**.
4. S. Suga, A. Sekiyama, M. Obara, J. Yamaguchi, M. Kimura, H. Fujiwara, A. Irizawa, K. Yoshimura, M. Yabashi, K. Tamasaku, A. Higashiya and T. Ishikawa, *Journal of the Physical Society of Japan*, 2010, **79**.
5. T. Toriyama, T. Nakayama, T. Konishi and Y. Ohta, *Physical Review B*, 2014, **90**.
6. M. Soltani, M. Chaker, E. Haddad and R. Kruzelecky, *Applied Physics in the 21st Century*, 2008, **661**.
7. Y. Ningyi, L. Jinhua and L. Chenglu, *Applied surface science*, 2002, **191**, 176-180.
8. Z. Wei and C. Gang, *Sino-Global Energy*, 2010, **6**.
9. A. V. D. Evgheni Strelcov, Uday Lanke, ClayWatts,and Andrei Kolmakov,, *ACS Nano*, 2011.
10. P. A. Shaikh, D. Shi, J. R. D. Retamal, A. D. Sheikh, M. A. Haque, C.-F. Kang, J.-H. He, O. M. Bakr and T. Wu, *Journal of Materials Chemistry C*, 2016, **4**, 8304-8312.
11. J. M. Wu and W. E. Chang, *ACS Applied Materials & Interfaces*, 2014, **6**, 14286-14292.
12. B. Fisher and A. Ron, *Solid State Communications*, 1981, **40**, 737-739.